SolarPACES 2022, 28th International Conference on Concentrating Solar Power and Chemical Energy Systems
Analysis and Simulation of CSP and Hybridized Systems
https://doi.org/10.52825/solarpaces.v1i.675

Published: 08 Mar. 2024

Impact of DNI Forecast Quality on Performance Prediction for a Commercial Scale Solar Tower

Application of Nowcasting DNI Maps to Dynamic Solar Tower Simulation

Christian Schwager[1][https://orcid.org/0000-0002-4515-886X], Florian Angele[1][https://orcid.org/0000-0002-0313-0770], Bijan Nouri[2][https://orcid.org/0000-0002-9891-1974], Peter Schwarzbözl[3][https://orcid.org/0000-0001-9339-7884], Cristiano José Teixeira Boura[1][https://orcid.org/0000-0003-1854-1019], and Ulf Herrmann[1][https://orcid.org/0000-0002-6938-0860]

[1] Solar-Institut Jülich of FH Aachen University of Applied Sciences, Germany

[2] Institute of Solar Research, German Aerospace Center, Spain

[3] Institute of Solar Research, German Aerospace Center, Germany

Abstract. Concerning current efforts to improve operational efficiency and to lower overall costs of concentrating solar power (CSP) plants with prediction-based algorithms, this study investigates the quality and uncertainty of nowcasting data regarding the implications for process predictions. DNI (direct normal irradiation) maps from an all-sky imager-based nowcasting system are applied to a dynamic prediction model coupled with ray tracing. The results underline the need for high-resolution DNI maps in order to predict net yield and receiver outlet temperature realistically. Furthermore, based on a statistical uncertainty analysis, a correlation is developed, which allows for predicting the uncertainty of the net power prediction based on the corresponding DNI forecast uncertainty. However, the study reveals significant prediction errors and the demand for further improvement in the accuracy at which local shadings are forecasted.

Keywords: Process Prediction, DNI Forecasting, Nowcasting, Uncertainty Analysis, Molten Salt Receiver System, Dynamic Process Simulation, Cloud Passage Simulation, Operating Assistance, Model Predictive Control

1. Introduction and simulation setup

Process prediction and model predictive control methods are developed to optimize yield and costs of concentrating solar power (CSP) plants. Due to the fluctuating supply of solar energy, the use of forecasting data increases their potential. Available DNI (direct normal irradiation) forecasting data are usually based on satellites or all-sky imagers (ASI) and differ in temporal and spatial resolution as well as the forecasting uncertainty [1]. In order to investigate the implications regarding process prediction and model-predictive control (MPR) for molten salt solar towers (MST) measured and forecasted DNI maps from an ASI-based system [2] are applied to raytracing [3] and the resulting series of flux density distributions is imported into a dynamic prediction model of a 700 MW_{th} external receiver system [4]. The latter is simulated in Dymola® with detailed discretized modelling of the receiver (Absorber tubes) and also includes the combined feedforward and feedback temperature control as tested in the SolarTwo plant [5] as well as the commercially applied clear-sky mass flow control [5, 6].

2. Impact of DNI map resolution

In order to determine the required quality of the input data for a dynamic process prediction, i.e. DNI forecast data, the prediction model is simulated with input data of different spatial quality. In this sense, the resolution of a series of DNI maps is coarsened with two different clustering methods, as illustrated in Figure 1. The original data (a) are obtained from a recently developed nowcasting system. These data include, for every 30 s of the day, a set of DNI maps from lead time 0 (LT00), which is considered as reference, up to 20 min lead time (LT20) in 1 min increments. For this part of the study, only the reference maps (LT00) are applied.

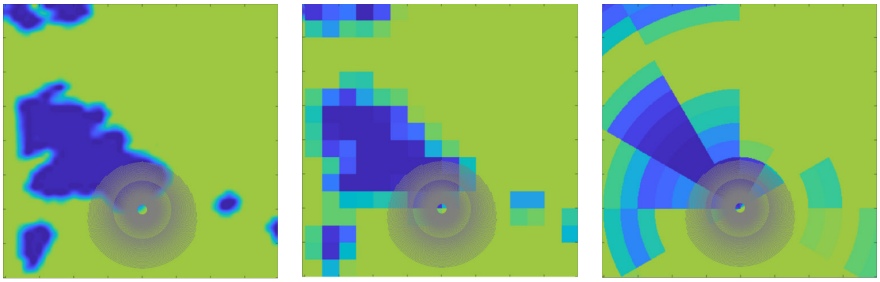

(a) (b) (c)

Figure 1. Visualization of (clustered) DNI maps and the heliostat field layout (a: original pixels 20 m by 20 m; b: Cartesian clustering 500 m by 500 m; c: polar clustering 30 ° by 500 m).

Since, in general, the available forecasting methods provide maps with different resolutions of square pixels, the Cartesian clustering method (Figure 1 b) enlarges the original 20 m by 20 m pixels to a multiple. Different enlargement factors are considered to replicate different forecasting methods, such as all-sky imager (high resolution) or satellite-based (lower resolution) systems. The clustering is done by calculating average values for each cluster to keep the integral within each cluster and for the entire DNI map consistent. In order to compare a clustering method that suits the heliostat field layout better, the polar clustering method is introduced, calculating average values across multiple pixels as well, but the aggregation is done on a polar coordinate-based pattern (compare Figure 1 c). The origin of the polar coordinate system is located at the tower position. The cluster sizes are varied in radial and circumferential direction independently from each other.

As a result, an excerpt of the predicted intercept and net power trends based on different input data resolutions (Cartesian method) are plotted in Figure 2. Significant deviation can be observed, especially with cluster sizes of more than 500 m. This is mostly due to averaging across areas that only partially intercept with the heliostat field so that outsider DNI values manipulate the simulated irradiance in the heliostat field.

In order to eliminate short-term deviations, which are irrelevant for predicting yield over a period of several minutes, a 20 min moving average is applied to the net power trends before calculating statistic metrics throughout a full operation day (10.5 h). The resulting mean-absolute deviation (MAD) and root-mean-square deviation (RMSD) are graphed in Figure 3 against the cluster size with (right) and without (left) applying the 20 min moving average. As expected, the RMSD rises progressively up to 5.4 MW_{el} at 2000 m wide clusters, but with decreasing cluster sizes, it converges to approx. 0.08 MW. Peak deviations reach from 0.25 MW_{el} to 16.15 MW_{el}. Regarding the model accuracy and the order in which prediction-based operational decisions can increase yield, it seems appropriate to aim for an RMSD of less than 1 % of the nominal power. Accordingly, a pixel size of less than 960 m is required to keep the RMSD below 1.2 MW_{el}. This excludes any state-of-the-art satellite-based forecasting technology, but the resolution of nowcasting maps from all-sky imager-based systems (ASI) is sufficient for such a yield prediction application.

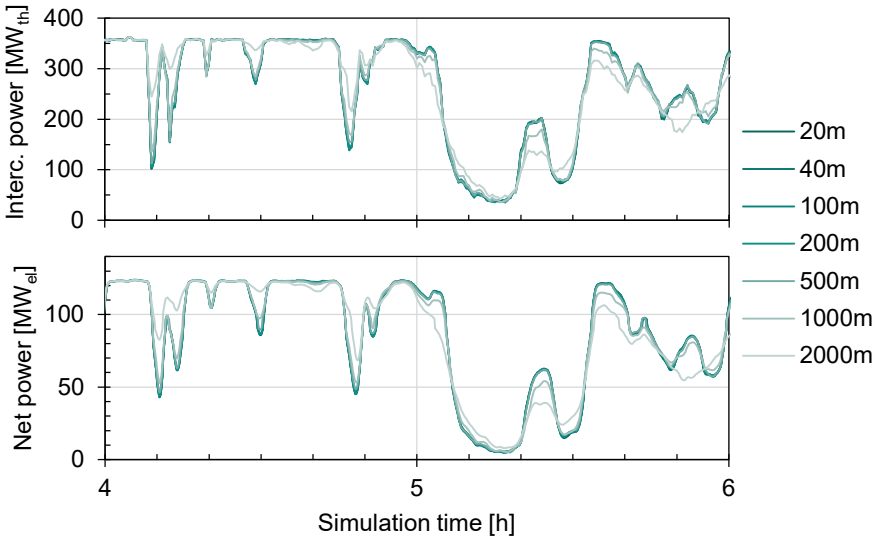

Figure 2. Excerpt of simulated intercept (top) and net (bottom) power based on different Cartesian cluster/pixel sizes.

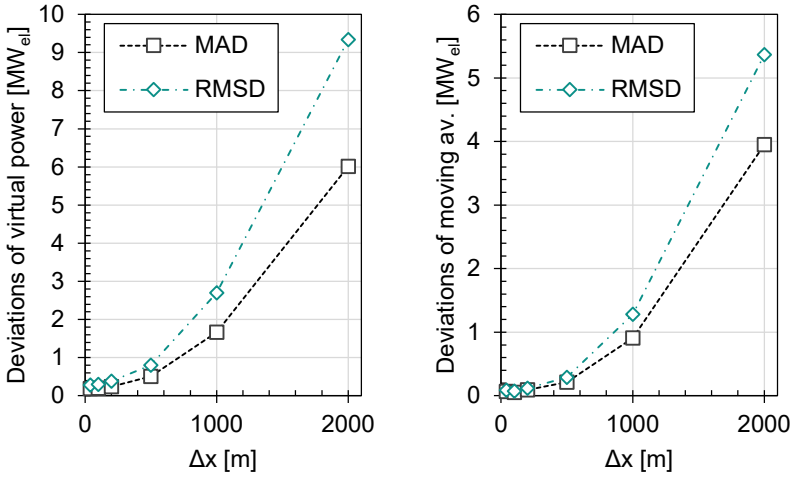

Figure 3. Statistics of the net power (left) and of the corresponding 20 min moving average (right) in dependence of the Cartesian cluster size.

Furthermore, the same statistical analysis is conducted for the polar clustering method to examine the influence of the heliostat field layout. The resulting MAD and RMSD values are plotted in Figure 4 against the circumferential (left) and radial (right) cluster sizes. In each of the two parameter variations, the respective other parameter is kept constant at the smallest considered value. Hence, the deviations are smaller compared to the Cartesian clustering. However, depending on the radial cluster size, the RMSD varies between 0.09 MW_{el} and 1.47 MW_{el} with a progressive trend, while peak deviations lie between 0.28 MW_{el} and 4.08 MW_{el}.

In contrast, the RMSD correlates almost linearly with the circumferential cluster size in the rage of 0.09 MW_{el} to 1.48 MW_{el} with peak deviations between 0.28 MW_{el} and 4.47 MW_{el}. In comparison, at small cluster sizes, the net power prediction is more affected by the circumferential resolution since the field efficiency and the receiver efficiency both vary around the circumference significantly, whereas the radial DNI gradients only interfere with the field efficiency and not with the receiver efficiency due to blurring effects caused by vertically offsetting aim points. However, at larger cluster sizes, the aforementioned impact of outsider DNI values (outside of the heliostat field but still within the cluster) explains the progressive increase in the dependency from Δr. With one additional parameter sweep for $\Delta\varphi$ at Δr =

500 m, it can be concluded that an appropriate cluster size of 500 m by 90 ° results in an RMSD of 0.79 MW_{el}.

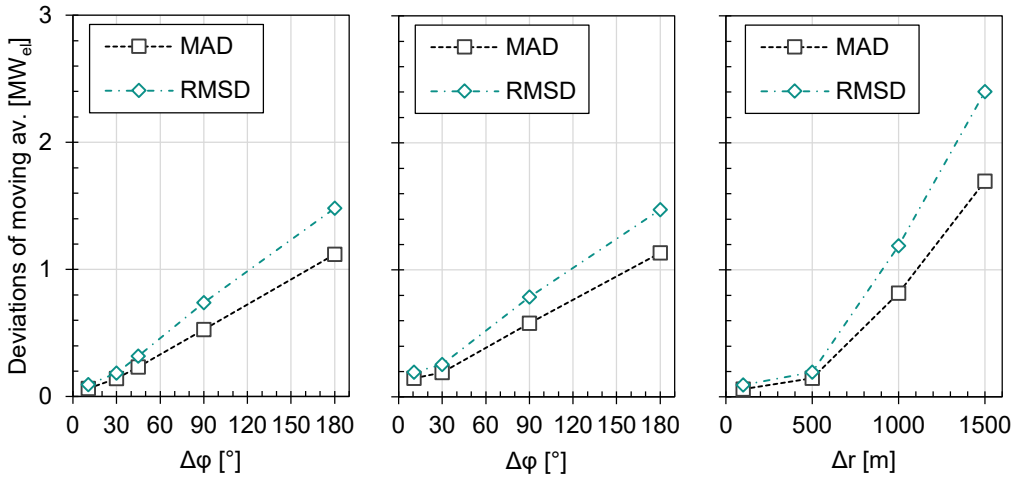

Figure 4. Statistics of the net power (20 min moving average) in dependence of the polar cluster size (Δφ at Δr = 100 m, Δφ at Δr = 500 m and Δr at Δφ = 10.6 °).

Moreover, the same analysis for the controlled outlet temperature results in the data shown in Figure 5. In addition to MAD and RMSD values, these plots include the maximal positive and negative deviation during the test scenario. Besides, these values are based on the actual predictions without temporal averaging since momentary deviations are relevant for control performance. These results clarify that coarse DNI map resolutions can lead to drastic over or underestimation of the outlet temperature. To keep the RMSD below 1 % of the nominal temperature span of 275 K, a pixel size of less than 370 m is required. Concerning the polar clustering, the outlet temperature prediction is much more sensitive regarding the circumferential cluster size, in contrast to the net power. This is plausible since circumferential flux gradients can cause significant outlet temperature variations even if they do not affect the overall intercept power. The sensitivity regarding the radial cluster size is only half as strong. Therefore, precisely forecasting the position of local shading is especially important concerning its azimuth relative to the tower. E.g., for a shadow that crosses the northern or southern part of the heliostat field the x position requires more accuracy than the y position. The opposite applies to partial shadings on the western or eastern part of the field. One additional parameter sweep over Δφ at Δr = 500 m suggests an appropriate cluster size of 500 m by 21.8 ° to achieve an RMSD of 2.75 K.

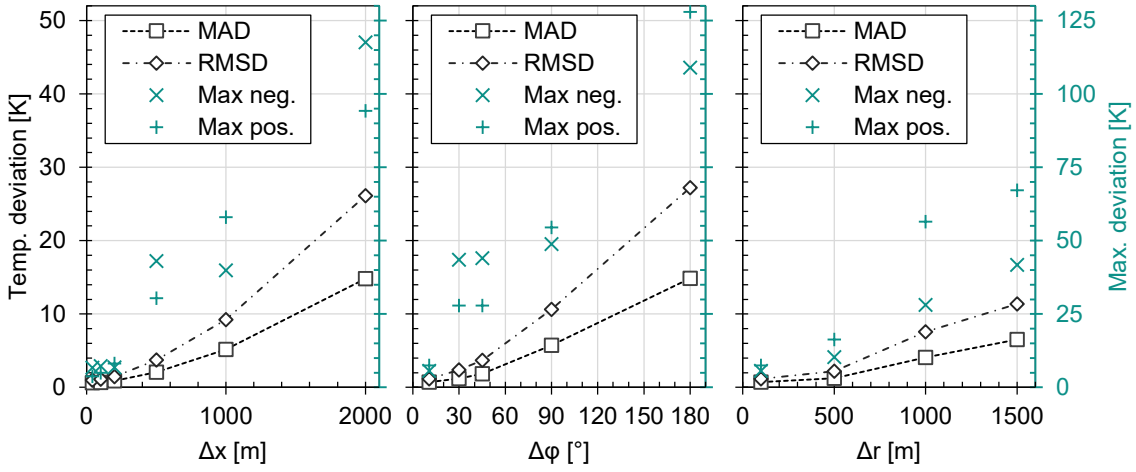

Figure 5. Statistics of the controlled outlet temperature in dependence of the Cartesian and polar cluster size (Δx, Δφ at Δr = 100 m and Δr at Δφ = 10.6 °).

3. Impact of DNI forecast errors on dynamic process prediction

In order to analyze how the dynamic simulation model performs with forecasted input data, including associated forecasting errors, designated forecasting scenarios with lead times from 0 to 20 are composed for the same day as above. I.e. the scenario LT20 represents a forecast based on ASI data from 20 min before each time step, whereas LT00 is considered as (auto validation) reference. As an example, Figure 6 shows the intercept and net power trends for LT01 to LT10 over 3 hours. Apparently, the shadow-induced drop-downs in the forecast scenarios are shifted to the right with increasing lead time. This is due to some shadows rather appearing and disappearing than moving across the heliostat field, making it difficult to forecast. Hence, the earlier the forecast is done, the older the data it is based on and therefore, the forecast is often lagging behind.

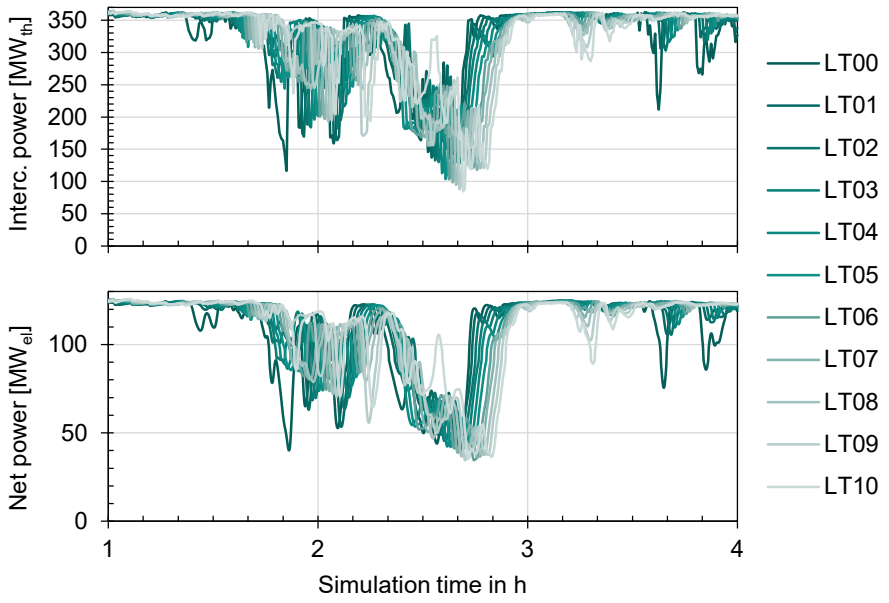

Figure 6. Excerpt of predicted intercept (top) and net (bottom) power based on forecasted DNI maps with different lead times.

The discrepancy between predicted and actual power becomes clearer in Figure 7, where the predicted (LT01) data is plotted against the actual (LT00) data. The intercept power scatters significantly and the net power data point agglomerate along circular paths, due to the thermal inertia. Ideally, they would all follow the indicated linear straight line. According to the plot below, the root mean square deviation (over time) of the intercept power lies around 35.8 MW_{th} with occasional deviations by more than 100 MW_{th} respectively for the net power around 11.2 MW_{el} with deviations up to approx. 30 MW_{el}. Those numbers significantly increase with longer lead times, but also decrease when applying a moving average on the power trends (see Figure 8). This is appropriate when the uncertainty of yield prediction for a certain period is of interest.

However, those results only represent one specific scenario and strongly depend on the achieved forecasting accuracy. To find a correlation between prediction and forecast uncertainty, the following study examines prediction errors in dependence of four different forecast error metrics. Since yield prediction is usually relevant for periods of several minutes, a 5 min moving average is applied on the power trends to mitigate short-term fluctuations. In addition, all forecast errors are calculated only based on pixels inside the heliostat field. First, the root mean square deviation (RMSD) over the heliostat field area is considered, as it is common in nowcasting validation. Second, the RMSD is applied on polar clustered (500 m by 90 °) DNI maps. Third, the absolute value of the bias (|bias|) is considered, which totally neglects spatial variations. Lastly, the bias itself is considered as the only signed error metric. Figure 9 presents the corresponding scatter plots with 95 % transparency and includes a

linear fit (dotted line). Apparently, the RMSD correlates poorly with the prediction errors as indicated by the low coefficients of determination (R^2). The clustered RMSD only achieves a minor improvement, whereas the (signed) bias results in the highest R^2.

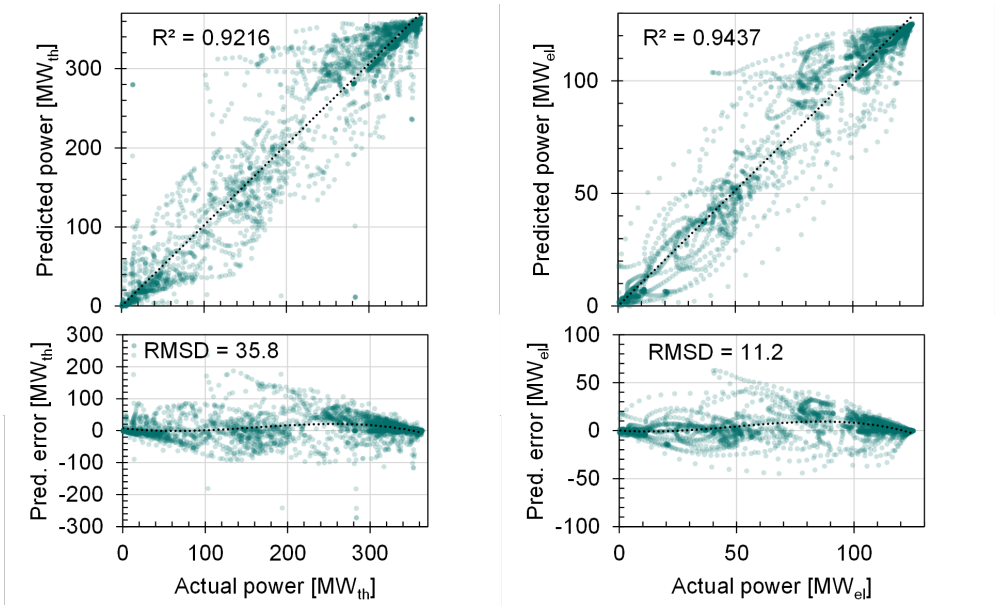

Figure 7. Predicted intercept (left) and net (right) power as well as the corresponding prediction errors scattered over actual power for 1 min lead time.

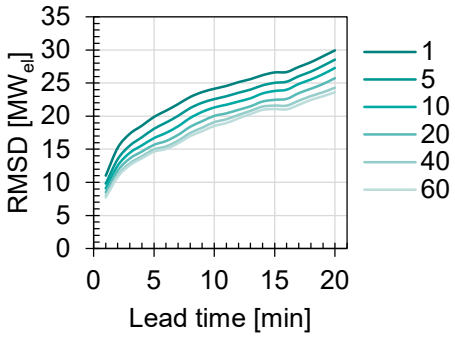

Figure 8. Sensitivity of the RMSD of the net power prediction over lead time with different moving average intervals.

Furthermore, each plot in Figure 9 includes a linear 95 % confidence threshold (dashed line), which can help to predict the uncertainty of power predictions at any time based on the corresponding forecast error in the following manner: With 95 % confidence

$$|\,prediction\ error\,| < a \cdot forecast\ error + b \tag{1}$$

with unsigned forecast error metrics respectively

$$a \cdot forecast\ error - b < prediction\ error < a \cdot forecast\ error + b \tag{2}$$

with the signed bios (compare Table 1). Moreover, the parameter *b* decreases with the mean average interval length. Hence, not only does the forecast and therefore prediction errors decrease with longer averaging intervals, but also its uncertainty can be predicted more precisely. Finally, as a performance indicator for the uncertainty prediction, the mean absolute value of the predicted uncertainty (MAPU) is given in Table 1 for the considered scenario and lead times in total. In conclusion, bios as a forecasting error metric results in the lowest MAPU and is therefore best suited for predicting the uncertainty of the net power prediction.

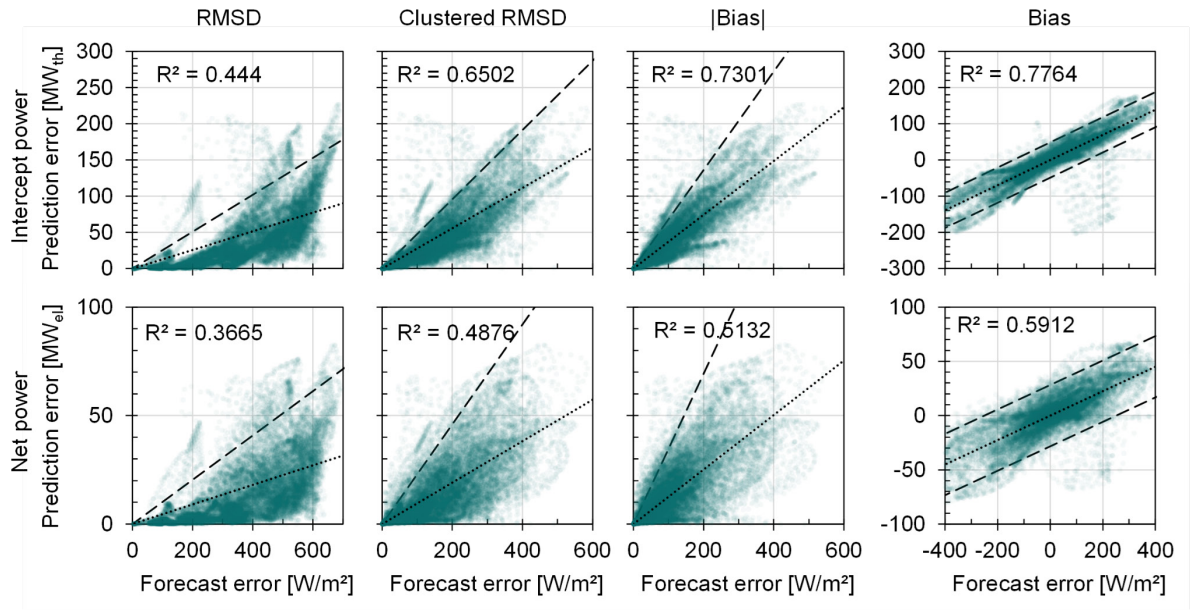

Figure 9. Prediction errors of the 5 min moving average of the intercept (top) and net power (bottom) values for all 20 lead times over different DNI map forecast error metrics.

Table 1. Parameters of the 95 % confidence threshold and resulting mean absolute uncertainty prediction (MAPU) for the net power prediction.

	$T_{mov.av.}$	RMSD-based	CRMSD-based	|Bias|-based	Bias-based
a, *b* [MW/(W/m²), MW]	5 min	0.102 , –	0.23 , –	0.3465 , –	0.1127 , 28.3
	20 min	0.0823 , –	0.1752 , –	0.231 , –	0.1223 , 16.4
	60 min	0.0755 , –	0.162 , –	0.2084 , –	0.1119 , 7.8
MAPU [MW]	5 min	38.2	37.7	40.6	28.6
	20 min	31.1	29.0	27.4	17.0
	60 min	29.1	27.6	25.5	8.0

The same uncertainty analysis for predicting the outlet temperature results in the plots shown in Figure 10. To make the results more relevant for model predictive control (MPR) the moving average interval is set to 1 min and only a lead time of 1 min is evaluated. However, all forecast error metrics correlate poorly with the outlet temperature prediction error.

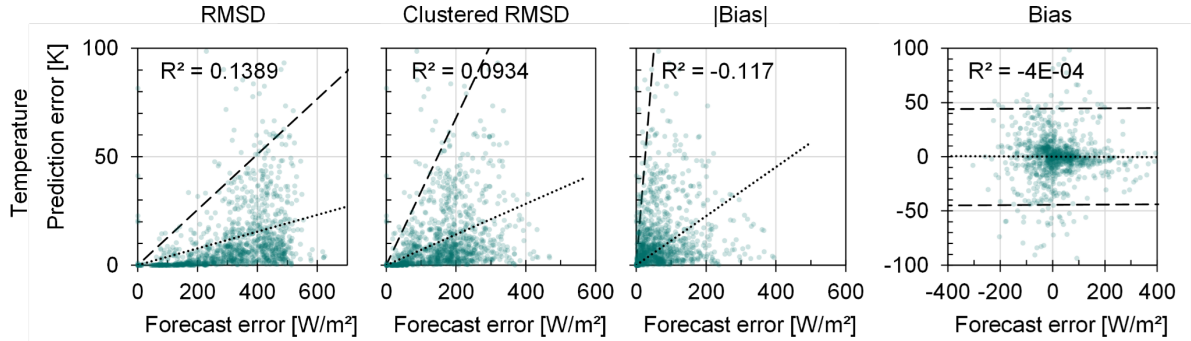

Figure 10. Prediction errors of the 1 min moving average of the receiver outlet temperature over different DNI map forecast error metrics.

4. Conclusion

Real nowcasting data respectively forecasted DNI maps were applied to a detailed dynamic prediction model of a full-scale molten salt receiver system coupled to a raytracing software in order to investigate the impact of DNI map quality and forecasting errors on receiver outlet temperature and net power prediction. The results indicate, that the DNI map resolution of a state-of-the-art ASI system is sufficient for both the outlet temperature and net power prediction. However, satellite-based systems would require further improvements to achieve pixel sizes in the order of hundreds of meters to achieve appropriate prediction accuracy.

Furthermore, a correlation developed based on a statistical uncertainty analysis allows for predicting the uncertainty of the net power prediction based on the uncertainty of the forecasted DNI maps, as it can be provided by the considered nowcasting system at any time for each pixel. The results also implicate the need for further improvements regarding the forecasting errors to allow for more accurate process predictions, especially for longer lead times. The use of forecasted DNI maps in model predictive outlet temperature control only seems reasonable, if local shadings can be forecasted more accurately.

Data availability statement

The applied data are subject to third-party IP and therefore not publically available.

Author contributions

Conceptualization[1], Data curation[1,3], Formal Analysis[1], Funding acquisition[1,5,6], Investigation[1], Methodology[1,2], Project administration[1], Software[1,2,4], Supervision[5,6], Visualization[1], Writing – original draft[1], Writing – review & editing[2,3,4,5,6]

Competing interests

The authors declare no competing interests.

Funding

This work is funded by the German Federal Ministry for Economic Affairs and Climate Action.

References

1. P. Heller, Ed., *The performance of concentrated solar power (CSP) systems: Analysis, measurement and assessment*. Duxford, Cambridge, MA, Kidlington: Elsevier, 2017. [Online]. Available: http://www.sciencedirect.com/science/book/9780081004470. doi: https://doi.org/10.1016/C2014-0-03695-7.

2. B. Nouri, N. Blum, S. Wilbert, and L. F. Zarzalejo, “A Hybrid Solar Irradiance Nowcasting Approach: Combining All Sky Imager Systems and Persistence Irradiance Models for Increased Accuracy,” *Solar RRL*, vol. 6, no. 5, p. 2100442, 2022, doi: 10.1002/solr.202100442.

3. N. Ahlbrink, B. Belhomme, R. Flesch, D. M. Quinto, A. Rong, and P. Schwarzbözl, “STRAL: Fast Ray Tracing Software With Tool Coupling Capabilities for High-Precision Simulations of Solar Thermal Power Plants,” in *Proceedings of the SolarPACES Conference 2012*, Marrakech, Marokko, 2012. [Online]. Available: elib.dlr.de/78440/

4. C. Schwager, F. Angele, P. Schwarzbözl, C. J. Teixeira Boura, and U. Herrmann, “Model Predictive Assistance for Operational Decision Making in Molten Salt Receiver Systems,” in *SolarPACES Conference 2021*, 2021.

5. R. Bradshaw *et al.,* “Final Test and Evaluation Results from the Solar Two Project,” Sandia National Laboratories, Albuquerque, New Mexico, 2002. doi: https://doi.org/10.2172/793226.

6. S. Relloso, “Noor III 150 MW Molten Salt Tower: 1st Year of Commercial Operation,” Casablanca, 2019.